The Astrophysical Journal, 660:1580–1587, 2007 May 10

ICE FORMATION IN RADIATED ACCRETION DISKS

Sanford S. Davis
NASA Ames Research Center, Moffett Field, CA 64035; sdavis@mail.arc.nasa.gov
Received 2006 August 10; accepted 2007 January 29

ABSTRACT

Gas to solid phase changes of abundant species in a viscous, irradiated protoplanetary disk are investigated using a new formulation for the freezeout effect. The method is based on a procedure using species-dependent phase diagrams while following the chemical evolution of water and carbon monoxide gas until their partial pressures are sufficient to de-sublimate vapor into ice. It is found that water ice is dominant throughout the nebula while a significant amount of water vapor coexists with the ice in the cooler parts of the inner nebula. Volatile CO molecules de-sublimate only in the colder outer regions of the nebula near the center plane. Computed column densities for CO gas are compared with similar calculations using an adsorption/desorption model by Aikawa and Herbst and are shown to predict similar distributions.

Subject headings: planetary systems: formation — planetary systems: protoplanetary disks

1. INTRODUCTION

Davis (2005) considered the migration of an evolving water-ice sublimation front in a two-dimensional axisymmetric protoplanetary disk. In the cited paper the condensation front location was computed for an evolving protoplanetary disk model. Over a period of about 10 million years the gas/ice boundary was shown to change significantly. No quantitative values of relative abundances of gases and solids were computed and only plausible assumptions were made regarding available abundances. In this paper, the condensation of gaseous material in the protoplanetary disk is considered in a quantitative manner using a more complete (but steady state) protoplanetary disk model where both the condensation front and the relative abundances of the considered species are computed in a self-consistent manner.

The present paper uses physical and chemical modeling to predict relative abundances of both ice and vapor in the colder regions beyond the sublimation front. This work includes a new formulation of the thermal adsorption/desorption process in the chemical network governing species evolution. This approach is different from the kinetic condensation/sublimation model commonly used, e.g., Aikawa et al. (1996) and Aikawa & Herbst (1999), but it will be shown that computed abundances are in reasonable agreement in regions where comparisons can be made.

The two species considered here are H_2O and CO. Water is a key component of protoplanetary disks and is also one of the most abundant species. It is a unique astrophysical substance since it undergoes critical phase changes in the middle regions of the solar nebula and, in its condensed state, may play a major role in terrestrial planet formation. Residual water vapor and water ice are found in planets, asteroids, and comets, which indicates water's ubiquitous nature. Carbon monoxide is chosen as the other species since it has a significant abundance ($\sim 10^{-5}$ relative to H) compared to other volatiles, has been definitely detected in several T Tauri stars (van Zadelhoff et al. 2001), and is expected to sublimate in the outer reaches of solar-type disks. It is demonstrated here how the disparate temperature/pressure environment in a protoplanetary disk affects both the equilibrium species abundance and the relative amount of H_2O and CO gas and ice.

Earlier work on chemical/physical processing in the nebula considered the inner nebula, and a series of papers dealing with aspects of high-temperature dust vaporization are available. The chemical evolution of silicate and carbon dust was considered by Duschl et al. (1996). They address phase changes of silicate dust from solid to gas phase at temperatures beyond 1500 K in the region near the central star. This work was expanded to include gas chemistry in addition to dust vaporization (Bauer et al. 1997), where they included the possibility of H_2O and CO vaporization in which these species are considered mantles on the dust particles. The model was extended to the outer nebula with a fixed water condensation front at about 10 AU and was reported by Willacy et al. (1998). All of this work used simple semianalytical active-disk models with an α-viscosity turbulence model.

The chemical evolution of molecular species in a one-dimensional protoplanetary disk including phase change processes on grains in the chemical network is considered by Aikawa et al. (1996). These models, now in common use, employ physics-based formulations where each adsorption or desorption term contains a number of free parameters (dust radius, sticking coefficient, etc.) that need to be chosen a priori. Here we bypass this step by using vapor pressure curves (similar to Duschl et al. 1996) for the adsorption/desorption process and make the assumption that the timescale for the phase change process is very fast compared to both chemical and evolutionary processes. The above cited physics-based adsorption/desorption process is extended to a two-dimensional model using a vertically isothermal disk (also with an α-viscosity model) by Aikawa & Herbst (1999).

Outer-disk modeling is now increasingly associated with a flared-disk model based on heating from a central star (or other nearby stellar sources). Rapid advances in this type of modeling followed research which advocated a simple two-layer model for an illuminated disk (Chiang & Goldreich 1997). This model was critically compared with more sophisticated radiative transfer procedures with the goal of predicting spectral energy densities (SEDs) of T Tauri or Herbig A/B stars (Dullemond & Natta 2003). Predicting SEDs from observational data continues to be a very important activity and a number of recent papers apply this basic formulation in increasingly more sophisticated ways. The radiative transfer method used by Dullemond et al. (2002) forms the basis of the passive (nonviscous) portion of the disk dynamics prediction code used in this paper. Here we use their basic formulation to study the disk's internal passive heating rather than as a source term to compute emitted SEDs. Internal viscous heating is included and is modeled using the β-viscosity model (Richard &

Zahn 1999; Davis 2002). This intense viscosity-based thermal source, which is important for chemical processing, is restricted to the midplane region of the inner part of the disk.

The plan of the paper is as follows: In § 2 the two-dimensional axisymmetric dynamic model is described and in § 3 the new sublimation model is introduced and related to the conventional adsorption/desorption approach. In § 4 the distributions of abundant species are compared and detailed vertical distributions of gas and ice are considered. In the final section the radial distributions of surface density for the species H_2O and CO are examined.

2. MODEL

In this section the underlying disk model is described followed by the gas-phase chemistry network adopted in this study. The last part of this section describes the new approach to gas/ice sublimation.

2.1. *The Dynamic Model*

The disk model used in this paper is based on the so-called fiduciary disk used in the two-dimensional α-disk modeling of D'Alessio et al. (1999). It represents a typical T Tauri star with a radius of 2 $R_\odot$, a mass of 0.5 $M_\odot$, and an effective temperature of 4000 K. The disk has a mass accretion rate of $10^{-8}\ M_\odot\ \mathrm{yr}^{-1}$ with an equivalent α-viscosity of 0.01. The center-line surface density and temperature (from the first figure of the cited reference) are indicated by long-dashed lines in Figures 1*a* and 1*b*. The current model requires such a surface density distribution as input. The surface density from the fiducial disk of Figure 1*a*, along with the stellar parameters, was used in the radiative transfer code described above, and the computed center-line temperature is indicated in Figure 1*b* by the solid line. These results show good agreement with the fiducial α-viscosity model and verify that both radiative transfer codes (with internal heating computed using different turbulent viscosity models) give similar results. The value of β used here was taken as 7×10^{-6} and was chosen to yield reasonable disk lifetimes as indicated by Davis (2002).

In order to compare computed column densities with the results of Aikawa & Herbst (1999), their simplified dynamic model was also considered and is given by the analytical formulas in equations (1) and (2) of the cited paper. The surface density distribution is based on a minimum-mass nebula model ($\Sigma \sim r^{-3/2}$) as commonly used in protoplanetary disk theory (Hayashi 1981), and is extended to two dimensions using a constant-temperature model at each radial station. The temperature distribution is a function of radius alone and is represented by an $r^{-1/2}$ power law. The surface density and temperature are also shown in Figures 1*a* and 1*b* as short-dashed lines. The main differences in the two formulations are the (unrealistically) high surface densities in the near-nebula and the constant-power-law slopes using the minimum-mass nebula. However, both models predict generally similar temperature profiles for $r > 10$ AU.

Computed two-dimensional temperature and number density distributions for the dynamic model are indicated in Figure 2. Here contours of temperature and number density exponent are presented in terms of $z/z_{\max}$ ($z_{\max}$ is the maximum value of the vertical grid at each radial station and is chosen as approximately 5 times the density scale height at each station) with log (r, AU) as abscissa. The ordinate is a rough angular measure of tan θ in a polar coordinate system centered at the central star and measured from the center line. The use of a logarithmic scale enhances the inner nebula. The short-dashed line represents density scale height and defines the region near the center plane (an included angle of about 22°) bounding about 80% of the disk mass. The long-dashed line defines the photospheric height defined as the vertical location

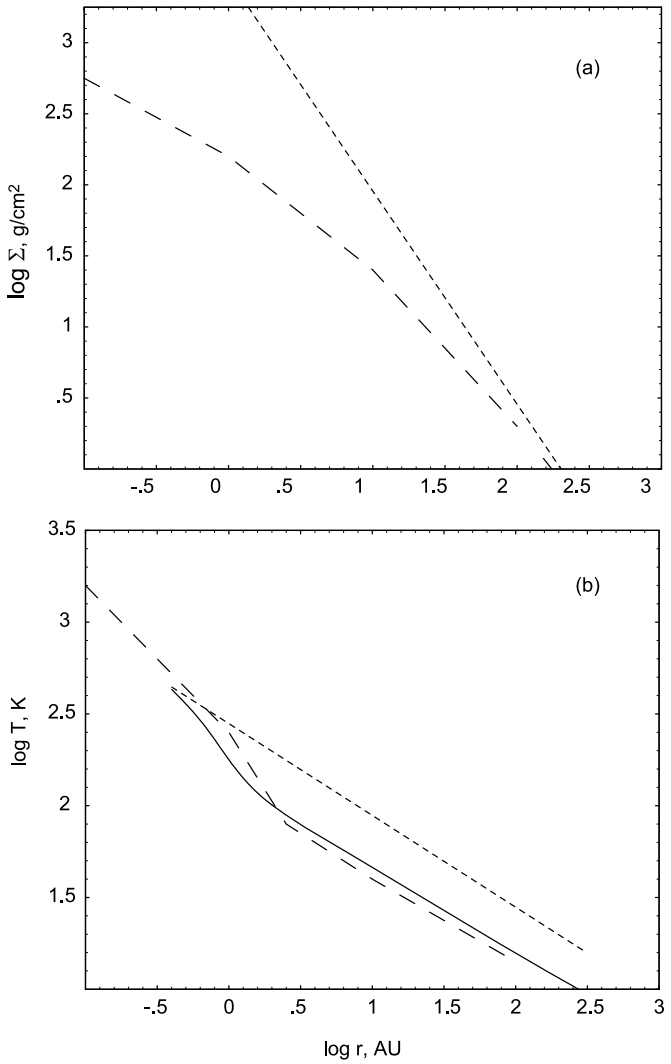

FIG. 1.—(*a*) Surface density and (*b*) center-plane temperature for the disk models considered in this paper. *Long-dashed lines*: Surface density and temperature from D'Alessio et al. (1999) using an α-viscosity model, $\alpha = 0.01$ (case 1). *Short-dashed lines*: Surface density and temperature from Aikawa & Herbst (1999) using a minimum-mass model (case 2). *Solid line*: Temperature computed from the input surface density given by D'Alessio et al. using a β-viscosity model, $\beta = 7 \times 10^{-6}$ (case 3). In cases 1 and 3, the stellar mass is 0.5 $M_\odot$, the stellar radius is 2 $R_\odot$, and the effective temperature is 4000 K. Case 2 represents a model with solar luminosity and mass.

where the optical depth is unity. It is computed from the density and a Rosseland mean opacity. The region below this line is the high-opacity area of the disk (e.g., $\tau > 1$).

The model shows vertical temperature inversions in the region 1–2 AU due to the competing effects of viscous and radiative heating. Two interesting observations from these contours are that (1) the photospheric height in the inner nebula approximately tracks the set of minimal radii for each temperature contour, and (2) the high-mass region below the curve of density scale height supports relatively constant temperatures at each radius. These boundaries can be interpreted as delineating the high-mass, high-opacity planet-forming regions of the disk from the more observable diffuse portion of the nebula. The former region is a small fraction of the disk energized by the central star, but includes most of the disk area influenced by internal heating. The outer diffuse region captures the low-optical-depth tenuous gas and is the main contributor to the observed disk. It is also the portion of the disk where photoionized species should predominate.

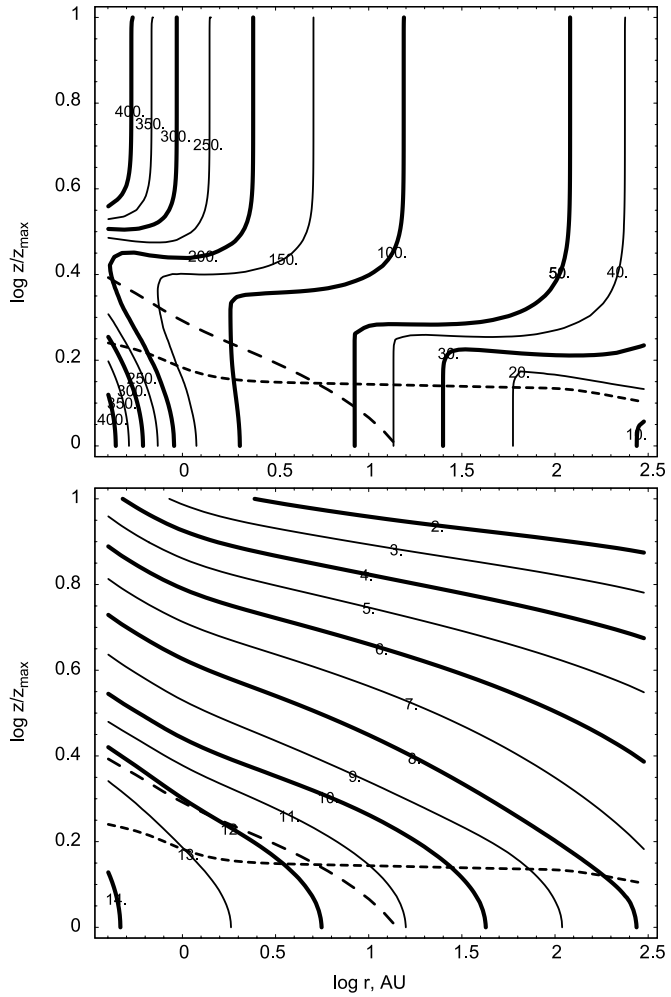

FIG. 2.—Contours of the temperature (K) and number density exponent (10^n cm^{-3}) for the nebula based on the fiducial disk model. The scale is chosen to delineate contours over a wide range of radii. The value of z_{max} is approximately 5 times the density scale height at each radius. The long-dashed line is the photospheric scale height (where the optical depth is 1), and the short-dashed line represents the density scale height.

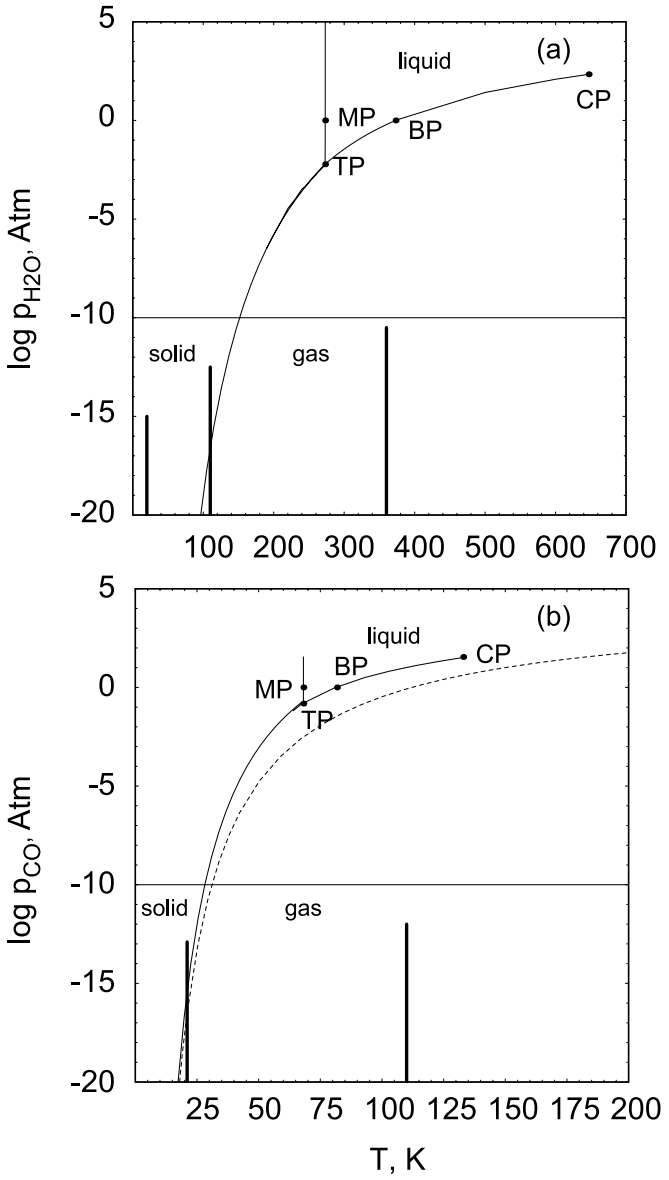

FIG. 3.—Phase diagrams for (*a*) water and (*b*) carbon monoxide. MP: Melting point. BP: Boiling point. TP: Triple point. CP: Critical point. Typical partial pressures for nebula species are well below these values and are represented by the region below $\log p = -10$. The vertical lines represent typical trajectories for the buildup of indicated species in the disk. The dashed curve in the bottom panel is derived from adsorption/desorption equilibrium for CO.

2.2. *The Chemical Network*

The evolution of gas-phase chemical species in the nebula is governed by a system of second-order (considering no more than two-body reactions) nonlinear ordinary differential equations. Such reaction networks include atomic and molecular collisions and a variety of ionizing reactions. They also require a large number of reaction coefficients that depend on the thermodynamic state at each point of the nebula and are typically gleaned from experimental databases or theoretical studies. Here we adopt the network known as the UMIST99 database, which consists of 396 species connected by 3740 reactions. The UMIST99 database for gaseous reactions includes the following components: two-body reactions using conventional chemical kinetics; photon induced reactions from the interstellar radiation field augmented by that from the central star with an exponential decay based on the local optical depth; and cosmic-ray reactions using an ionization rate $\zeta = 1.3 \times 10^{17}$ s^{-1}. Surface formation of hydrogen molecules on grain surfaces is also included. The only input to the network is the local temperature and density from the dynamic model along with initial abundances. These are taken as elemental solar abundances whose major constituents are in the ratio $\mathrm{H:O:C:N} = 1:9.2 \times 10^{-5}:4.4 \times 10^{-5}:2.0 \times 10^{-5}$, and all molecular species form naturally during the evolutionary process.

A new feature added to the network is an evolutionary sublimation model to predict the phase change of H_2O and CO molecules from gas to solid state. The important freezeout processes for these abundant species use the new model described in the following section. This phase-diagram-based condensation model replaces the conventional thermal adsorption/desorption process.

2.3. *The Sublimation Model*

With regard to the sublimation model, a central role is played by the phase diagram. Phase diagrams for water and carbon monoxide are shown in Figures 3*a* and 3*b*, respectively. The four critical points for terrestrial conditions are indicated for reference. The operating range in a disk is log p below -10 (*horizontal line*) and is orders of magnitude below the critical points. Here the phase

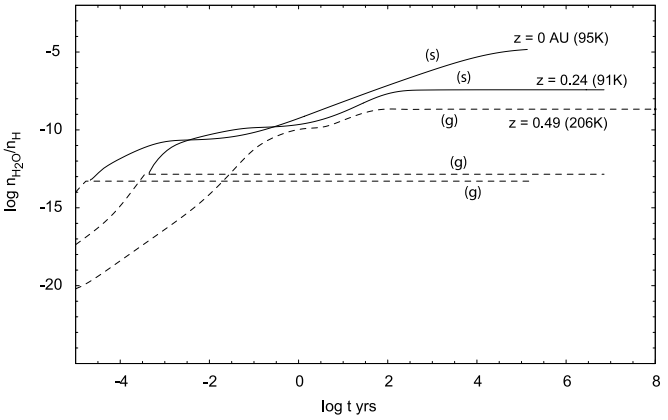

FIG. 4.—Chemical evolution of gas/ice at $r = 2.2$ AU showing time-variable phase changes at two elevations (high abundance of ice and low abundance of gas at large times) and the presence of vapor alone at $z = 0.49$ AU. The three temperatures are 95, 92, and 206 K, respectively, for this fiducial disk model. *Solid lines*: Solid phase. *Dashed lines*: Gas phase.

change will consist of a freezeout from gas to solid at a particular time during chemical evolution. Since the sublimation curves are almost vertical here, a commonly quoted parameter is the sublimation temperature of about 120 K for water and 25 K for CO. In reality the phase diagram has a finite curvature and there is a weak dependence on partial pressure. This mild pressure dependence determines the critical abundance of H_2O and CO where freezeout occurs since molecular abundances are vanishingly small at the initial time and slowly build to their final values.

The basic procedure is to compute freezeout by advancing the chemical network until the partial pressure of the considered species reaches the sublimation curve from below. At this point the gaseous abundance is fixed at this freezeout value. As the network continues to generate an incremental gaseous species, it is instantaneously converted to the ice phase. This assumes that the timescale for condensation is small compared with that for chemical evolution, which is generally true (Duschl et al. 1996). In this manner the ice abundance builds up to its steady state value and gas abundance remains at the critical value. The relative proportion of vapor and ice depends on local thermodynamic conditions and may vary widely over the nebula. It should be noted that sublimation process removes water and carbon monoxide molecules from the network, so the gaseous components of these species are reduced accordingly. The elements contained in the frozen-out molecules are no longer available in their original elemental gaseous abundances and these reductions can affect other carbon and oxygen containing species in the network.

Figure 3*a* shows the freezeout effect for H_2O vapor at three typical operating conditions shown by vertical lines at 20, 110, and 360 K. These temperatures represent conditions in the outer, mid-, and inner nebula. (In an evolving nebula these trajectories would be curved lines.) The height of each line indicates the buildup of water molecules to water's steady state abundance from its initial condition $\log p = -\infty$. In the outer nebula the vast preponderance is water ice (piercing of the sublimation curve at very low partial pressures). However, in the mid-nebula the gas-ice boundary appears during chemical evolution and the gas partial pressure can be quite high. The point where the sublimation curve is first breached determines the partial pressure of water vapor at that position. In the inner nebula, water ice is absent and only water vapor appears. The curve for CO in Figure 3*b* is typical of highly volatile species. The two vertical lines depict trajectories at 24 and 110 K in the outer and mid-nebula.

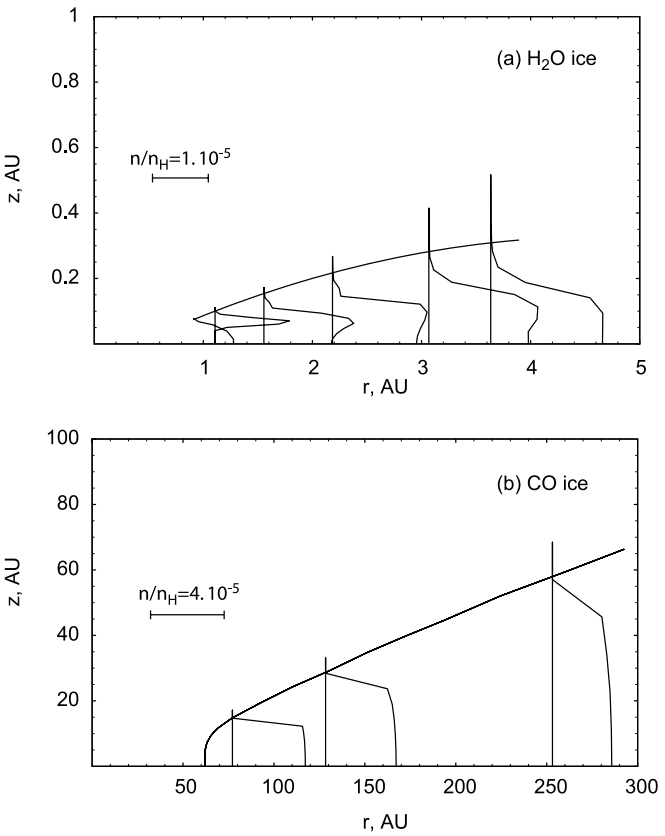

FIG. 5.—Inset plots of (*a*) H_2O ice and (*b*) CO ice abundances. In each case the boundary separating vapor from ice is shown with the curved line. Here (*a*) highlights the inner part of the nebula and (*b*) emphasizes the CO ice formation region in the colder outer regions of the disk.

The line corresponding to the far-nebula pierces the sublimation curve at a low partial pressure and CO ice is, as expected, the most abundant phase. However, there is always a small amount of CO gas at these cold temperatures. Simple models that use a sublimation temperature alone will not capture this effect.

Figure 3*b* also compares the vapor pressure curve for CO with that obtained from adsorption/desorption processes. Following the presentation given, for example, in Aikawa et al. (1996) the competing effects of adsorption and desorption are modeled using the physics-based formulation

$$A - D = \pi a^2 n_{\rm grains} S \sqrt{\frac{8kT}{\pi M_i}} n_i - n_{\rm des} \nu_{\rm osc} e^{-E_i/kT}.$$

The first term represents adsorption of species i with mass M_i onto grains and depends on a number of (not all well documented) parameters. The second term represents desorption of the particular species in terms of an "oscillator model" and an exponential factor representing the desorption energy. Assuming $n_{\rm grains} = n_{\rm des}$ the vapor pressure curve is obtained from setting $A = D$. Using typical parameters from the cited reference, an equivalent adsorption/desorption vapor pressure curve for CO is obtained. It is shown by the dashed curve in Figure 3*b* and tracks the vapor pressure curve quite well over the operating range considered.

3. RESULTS

3.1. *Ice and Vapor Abundances*

An example of the freezeout effect in an evolving chemical network is indicated in Figure 4, which shows time histories of water

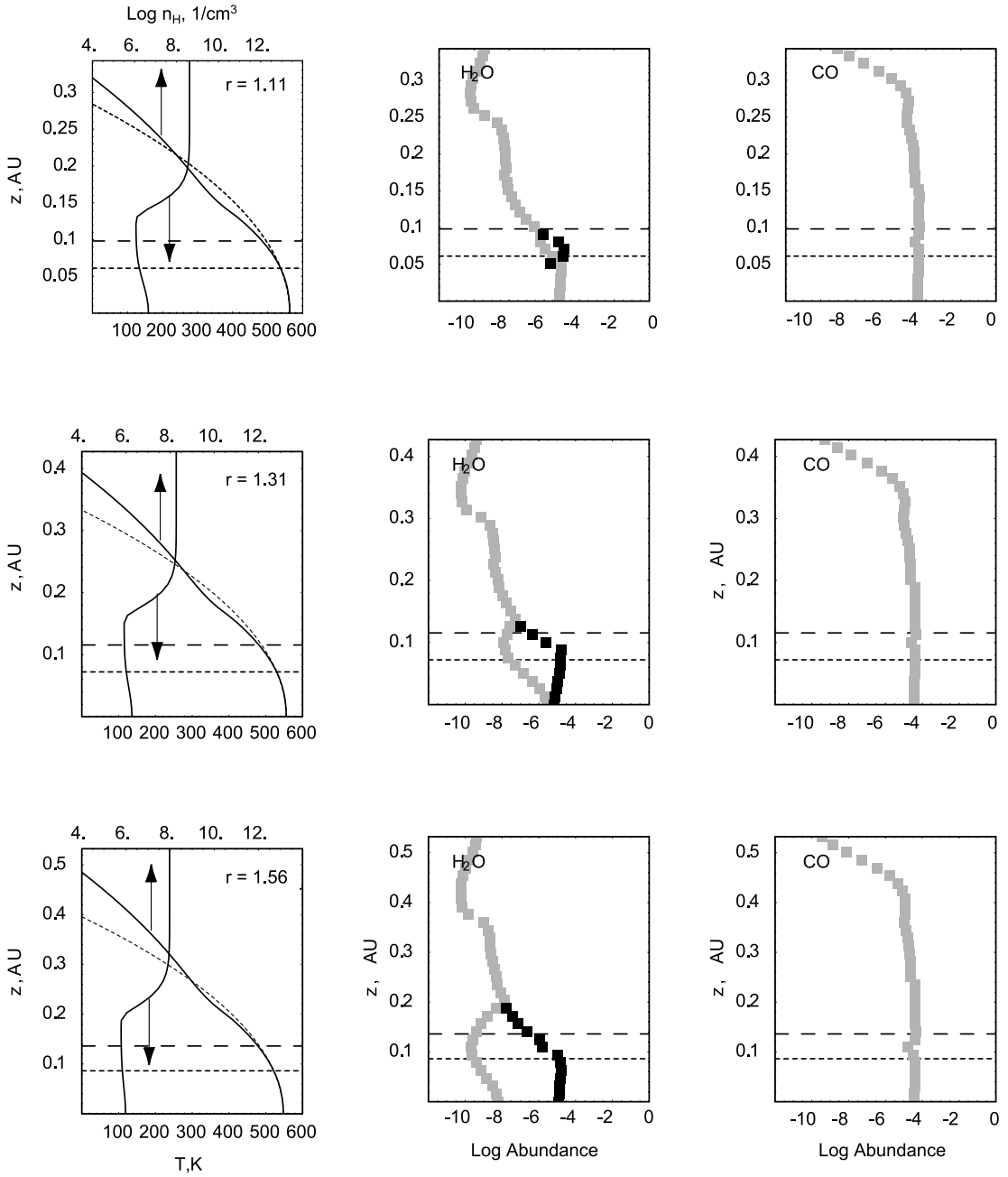

FIG. 6.—Vertical distribution of steady state gas (*gray symbols*) and ice (*black symbols*) at three radial locations in the near-nebula. *Left panels*: Temperature and number density profiles. The number densities are compared with the constant-temperature approximation (*short-dashed curve*). Density and photospheric scale heights are shown by short- and long-dashed lines, respectively. *Middle panels*: Vertical distribution of water abundance. *Right panels*: Vertical distribution of CO abundance.

molecules at 2.2 AU for three elevations with temperatures of 95, 91, and 206 K, respectively. The phase change from gas (g) to solid (s) occurs at different times. In this case the phase change occurs very early in the evolution for the two lower elevations. The final steady state abundances (relative to hydrogen atoms) are (1) $z = 0$, $n = 5.1 \times 10^{-14}$ (g), 1.5×10^{-5} (s); (2) $z = .24$, $n = 1.4 \times 10^{-13}$ (g), 3.8×10^{-8} (s); and (3) $z = .49$, $n = 2.14 \times 10^{-9}$ (g), 0.0 (s). In this inner-disk example the ice extends from the center line to an upper boundary at about 0.30 AU. At other radii the ice may form a cloud between two intermediate elevations. This effect is shown in Figure 5.

Figure 5*a* shows profiles of water-ice abundances as insets at a number of radial stations in the region $r < 5$ AU bounded by the condensation front. The ice sublimation front in the region near 1 AU is interesting. A cloud layer of ice covers the center plane, which is itself heated by viscous body forces. Above the ice layer the gas is heated by stellar radiation, especially where the optical depth is less than 1. The condensation front has two branches: a short segment from $r = 0.95$–1.3 AU where it intersects the center plane, and an extended branch that grows and eventually encompasses the entire disk below the photosphere. The two branches meet at a cusp. This two-branched structure is similar to that computed for the evolving nebula in Davis (2005) and approximates the evolutionary state from that paper at a time of about 10^6 yr. The inset profiles show the spatial evolution of ice abundances. The spatial gradient of ice abundance is quite large in the region near the condensation front, and mass diffusion effects can be important. This possibility is investigated by Cuzzi & Zahnle (2004)

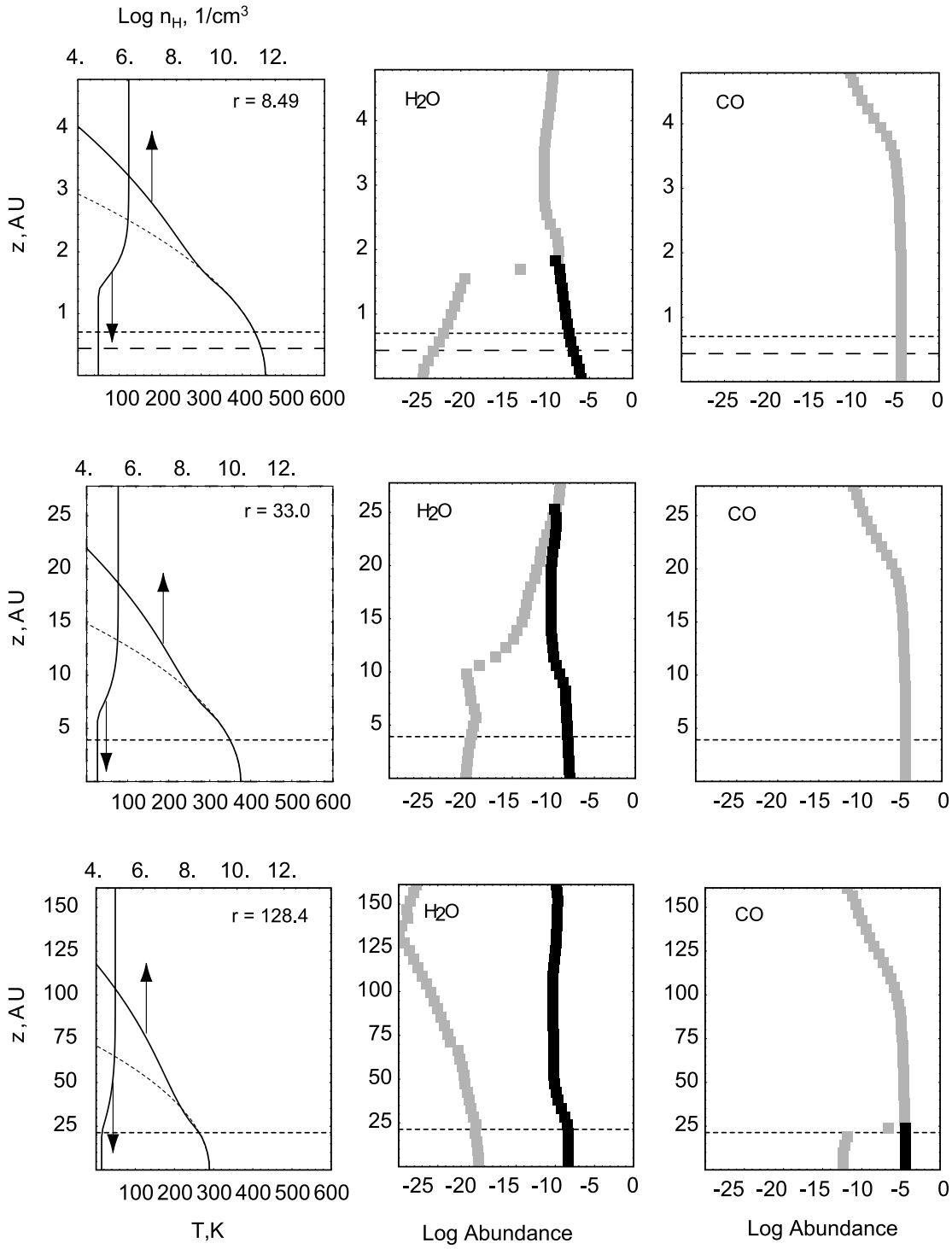

FIG. 7.—Vertical distribution of steady state gas (*gray symbols*) and ice (*black symbols*) at three radial locations in the mid- and far-nebula using the same notation as Fig. 6.

using these large horizontal gradients as a possible migration path for water and other volatiles. They show that large ice gradients in the vicinity of the front induce vapor phase enhancement in the hotter region closer to the central star. They surmise that this effect can contribute to the planet-building process in this region.

From Figure 5*a* a local peak ice-abundance maximum appears above the center plane and evolves into a monotonically decreasing profile that slowly decays with radial distance but grows in vertical extent. Figure 5*b* shows the condensation front for CO and is characteristic of less volatile species. Here the condensation front first appears at much higher radii and is a smooth one-branched curve, and the maximum CO abundance decays monotonically along the center plane. In this case the gaseous regime predominates except in the center-plane region at radii greater than about 50 AU. The pattern at these large radii is to have ice regions up to and slightly above the density scale height overlaid by an extensive region of gaseous CO.

Vertical profiles of gas/ice abundances at representative near-, mid-, and far-nebula regions are shown in Figures 6 and 7. The middle panels of Figure 6 show the radial transition from the first

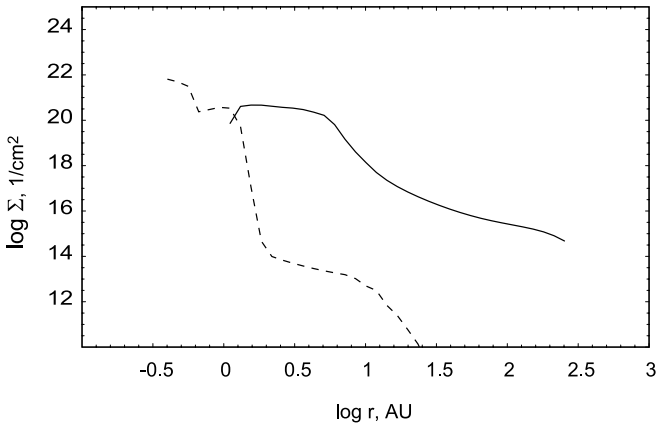

FIG. 8.—Radial distribution of gas (*dashed curve*) and ice (*solid curve*) column densities for water species. Note the domination of ice species in the region beyond 1 AU.

appearance of water ice in the inner part of the nebula at 1.11 AU to extensive icy regions at 1.56 AU. The right panels indicate the predominance of CO vapor at these near-field stations. The left panels show the temperature and density profiles at these radial stations. The thermal profile contains an inversion with its minimum near the photospheric height (*long-dashed line*) which, at these radii, is greater than the density scale height (*short-dashed line*). A simple, constant-temperature exponential number density profile (Willacy & Langer 2000; Aikawa & Herbst 1999) is shown by the short-dashed curve. This result shows that the simplified number density model is certainly adequate in this inner, dense, and optically thick part of the disk. The water vapor/ice profiles are indicated in the middle panels with ice as black symbols. At 1.11 AU the abundance of water vapor is relatively constant at 10^{-5} $n_{\rm H}$ below the density scale height and is reduced to about 10^{-8} $n_{\rm H}$ above the photosphere. An ice cloud is just starting to appear in the region between the density and photospheric scale heights that is close to the temperature minimum. This is the level where warming from viscous heating (from below) and stellar heating (from above) are minimal. At $r = 1.31$ and 1.56 AU the ice layer expands in both directions and the lower limb extends to the center plane. With further distances the ice expands in the vertical direction (cf. Fig. 5*a*). In this near-field ice region the gas/ice ratio is significant as both phases appear in relatively high abundances. The CO abundance, as expected, is entirely gaseous and is relatively constant at a value of about 10^{-4} $n_{\rm H}$ in both radius and elevation except in the higher, tenuous regions of the disk.

Figure 7 shows profiles farther out in the nebula. In the mid- to far-nebula the density scale height exceeds the photospheric height, and by 33 AU the optical depth is less than 1 throughout the nebula. The temperature profiles are essentially flat in the planet-forming, high-density region near the midplane where the number density is also well approximated by an exponential error function profile. The center-plane temperature is quite cold and there is no inversion of the temperature profile since viscous heating is ineffective at these distances and most of the heating is attributed to stellar radiation at higher elevations. Water-ice abundance is extensive and ice extends from the center plane to much larger altitudes. This is expected based on the lower center-plane temperature. The net effect is that the gas/ice ratio becomes extremely small and is reduced by as much as 10 orders of magnitude at some elevations. Only high above the center plane does gaseous water exist in abundances close to that of ice. The CO is entirely gaseous except at large distances where CO ice forms at the center plane. The surface density of CO at these large radii has contributions from both

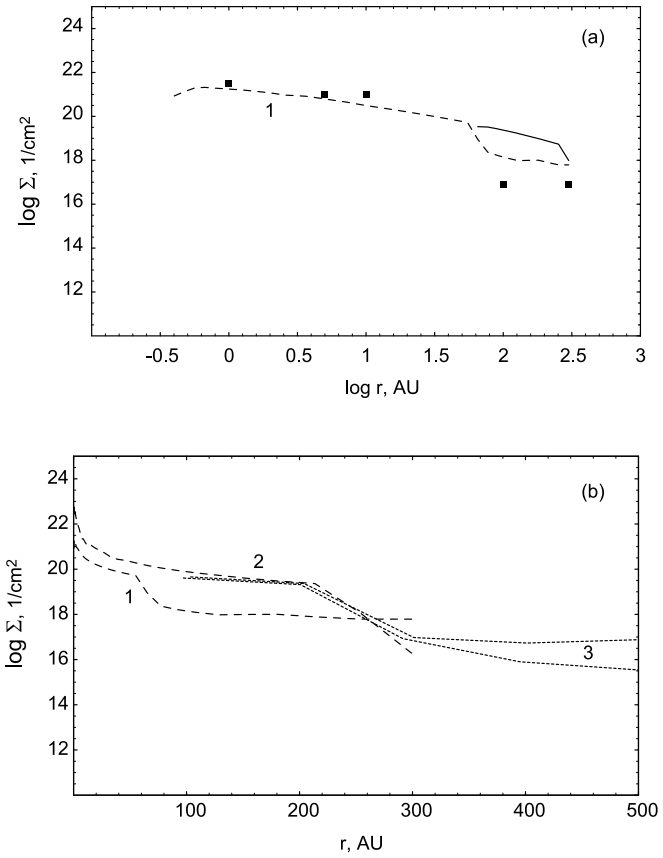

FIG. 9.—Radial distribution of CO surface densities. (*a*) Comparison of gas (*dashed curve*) and ice (*solid curve*) with calculations from Markwick et al. (2002) and Willacy & Langer (2000). (*b*) Far-field comparison with gas-phase calculations from Aikawa & Herbst (1999). *Curve 1*: Fiducial disk model. *Curve 2*: Aikawa-Herbst model. *Curve 3*: Range of CO abundances using the minimum-mass disk model of Aikawa & Herbst (1999).

gas and solid phases and, along with water surface density, is considered in the following section.

3.2. *Ice and Vapor Surface Densities*

The radial distribution of water column density has some interesting features. Starting from small radii, the apparent steplike behavior for gaseous water in Figure 8 (*dashed line*) is due to the enhanced temperature inversion at these smaller radii (cf. Fig. 2). Numerical simulations show that the point of minimum temperature serves as a species discriminator whereby diverse oxygen containing compounds can form in the chemical network at different levels depending on the local temperature (and weakly on the number density). For example, at 0.4 AU ($\log r = -0.4$, $z_{\rm max} = 0.093$ AU) the predominant oxygen-containing species is water vapor for $0 < z/z_{\rm max} < 0.22$; CO for $0.22 < z/z_{\rm max} < 0.43$; atomic oxygen for $0.43 < z/z_{\rm max} < 0.86$; and finally water vapor again at larger altitudes. These species are well correlated with the temperature variations around the minimum at $z/z_{\rm max} = 0.43$. Thus, at each radius the contribution to water vapor changes in a ways that results in the vertically integrated gas-phase curve in Figure 8 for $\log r < 0$. At larger radii the temperature drops below that required for water sublimation, and the predominant species at all levels is water ice, as indicated by the solid curve. In the region near 1 AU there is mixture of ice and vapor in almost equal proportions. In the far-nebula the ice abundance exceeds the gaseous component by many orders of magnitude. In a recent paper Dominik et al. (2005) show how it is possible to get water vapor

in the far-nebula. In that case other photodesorption processes are invoked and regions far above the center plane are considered.

The column density for CO in Figure 9*a* shows a very different behavior. In the logarithmic scale of Figure 9*a* the slow growth to a peak at about 1 AU is attributed to the presence of other carbon compounds due to the wide range of temperatures encountered in this region. In general a variety of carbon- and oxygen-containing species appear in the region <1 AU where the temperature is less than that required to vaporize the dust (Bauer et al. 1997). Species such as CH_4, C_2, and HNC with abundances greater than CO may appear. There is also a large population of carbon ions in the upper region of the inner nebula. All these effects tend to increase the CO surface density as the temperature decreases with increasing radius. Beyond 1 AU the CO abundances remain high and relatively constant while the surface density decreased uniformly due to the decreasing overall density. At about 55 AU CO freezeout occurs and a mixture of gas and ice remains to large radii. From Figure 7*a* the CO ice is overlain by a large (but diffuse) region of CO vapor at all larger radii, so both phases contribute to the overall surface density but ice predominates due to its location in the dense center plane. The symbols show computed gaseous CO surface density data from Markwick et al. (2002) and Willacy & Langer (2000). These authors use a variety of modeling techniques, but the general trends are similar in all cases.

In Figure 9*b* the surface density is compared directly with computations (using a linear scale in the *r*-direction) by Aikawa & Herbst (1999), who calculate CO gas abundances in the far-nebula region. Their model consisted of an exponential surface density and constant temperature at each station and differs from the current model as illustrated in Figure 1. Curve 1 is the predicted CO gas column density using the "fiducial disk," and the sublimation front is indicated at about 55 AU. This station is much less than the value of 200 AU predicted by the Aikawa & Herbst model, as indicated by the pair of short-dashed curves 3 showing the range of values from the cited paper. This is another instance of the difficulty of comparing the wide variety of coupled chemical/dynamic models used in chemical evolution modeling (Markwick et al. 2002). The CO gas column density was recomputed using the Aikawa & Herbst dynamic model and the same chemical evolution model as curve 1. The calculation is shown as dashed curve 2 and indicates good agreement up to and including the sublimation front at 200 AU. This result shows that the simplified condensation model used here is fully consistent with the adsorption-desorption model.

4. CONCLUSIONS

This paper showed how a simplified phase change model can be included in the chemical evolution process to predict relative abundances of both gaseous and solid components. With respect to water ice in the nebula, its maximum abundance must be no greater than about 4×10^{-5} since the abundance of water molecules must not exceed levels of atomic oxygen. These additional water-ice opacity sources may be important as its spatial distribution can affect the local optical depth, which in turn can affect the temperature. This feedback effect will be considered in future work.

The carbon monoxide abundance is found to coexist in both solid and gaseous form in the outer nebula. CO ice predominates in the center-plane region. Since CO gas is one of the commonly measured species in protoplanetary disks, the gas column densities can be a useful gauge to determine ice abundances in the outer nebula. This ice (in addition to water ice) is also an important component of cometary nuclei, which presumably forms in the colder regions of the nebula.

In this model supersaturation was not included, but it can be easily implemented with a modified vapor pressure curve. Additional freezeout of additional species would only require implementing the relevant phase diagrams.

I would like to thank an anonymous reviewer for important suggestions regarding this paper. This work was partially supported by the NASA/Ames Astrobiology Program.

REFERENCES

Aikawa, Y., & Herbst, E. 1999, A&A, 351, 233
Aikawa, Y., Shoken, M. M., Nakano, T., & Umebayashi, T. 1996, ApJ, 467, 684
Bauer, I., Finocchi, F., Duschl, W. J., Gail, H.-P., & Schloder, J. P. 1997, A&A, 317, 273
Chiang, E. I., & Goldreich, P. 1997, ApJ, 490, 368
Cuzzi, J. N., & Zahnle, K. J. 2004, ApJ, 614, 490
D'Alessio, P., Calvet, N., Hartmann, L., Lizano, S., & Canto, J. 1999, ApJ, 527, 893
Davis, S. S. 2002, ApJ, 576, 450
———. 2005, ApJ, 620, 994
Dominik, C., Ceccarelli, C., Hollenbach, D., & Kaufman, M. 2005, ApJ, 635, L85
Dullemond, C. P., & Natta, A. 2003, A&A, 408, 161
Dullemond, C. P., van Zadelhoff, G. J., & Natta, A. 2002, A&A, 389, 464
Duschl, W. J., Gail, H.-P., & Tscharnuter, W. M. 1996, A&A, 312, 624
Hayashi, C. 1981, Prog. Theor. Phys. Suppl., 70, 35
Markwick, A. J., Ilgner, M., Millar, T. J., & Henning, Th. 2002, A&A, 385, 632
Richard, D., & Zahn, J.-P. 1999, A&A, 347, 734
van Zadelhoff, G. J., van Dishoeck, E. F., Thi, W. F., & Blake, G. A. 2001, A&A, 377, 566
Willacy, K., Klahr, H. H., Millar, T. J., & Henning, Th. 1998, A&A, 338, 995
Willacy, K., & Langer, W. D. 2000, ApJ, 544, 903